Geophysical Research Letters

RESEARCH LETTER
10.1029/2020GL089576

Injection-Induced Seismic Moment Release and Laboratory Fault Slip: Implications for Fluid-Induced Seismicity

Lei Wang[1,2], **Grzegorz Kwiatek**[1], **Erik Rybacki**[1], **Marco Bohnhoff**[1,2], **and Georg Dresen**[1,3]

[1]Helmholtz Centre Potsdam, GFZ German Research Centre for Geosciences, Potsdam, Germany, [2]Department of Earth Sciences, Free University Berlin, Berlin, Germany, [3]Institute of Earth and Environmental Science, University of Potsdam, Potsdam, Germany

Key Points:
- Injection-induced fault deformation is dominantly aseismic
- Total moment release depends on total injected volume, independent of fault slip behavior
- Moment-injected volume scaling is linear for stable slip but shows a cubic relation for dynamic slip

Supporting Information:
- Supporting Information S1

Correspondence to:
L. Wang,
wanglei@gfz-potsdam.de

Citation:
Wang, L., Kwiatek, G., Rybacki, E., Bohnhoff, M., & Dresen, G. (2020). Injection-induced seismic moment release and laboratory fault slip: Implications for fluid-induced seismicity. *Geophysical Research Letters*, *47*, e2020GL089576. https://doi.org/10.1029/2020GL089576

Received 1 JUL 2020
Accepted 17 OCT 2020
Accepted article online 26 OCT 2020

Abstract Understanding the relation between injection-induced seismic moment release and operational parameters is crucial for early identification of possible seismic hazards associated with fluid-injection projects. We conducted laboratory fluid-injection experiments on permeable sandstone samples containing a critically stressed fault at different fluid pressurization rates. The observed fluid-induced fault deformation is dominantly aseismic. Fluid-induced stick-slip and fault creep reveal that total seismic moment release of acoustic emission (AE) events is related to total injected volume, independent of respective fault slip behavior. Seismic moment release rate of AE scales with measured fault slip velocity. For injection-induced fault slip in a homogeneous pressurized region, released moment shows a linear scaling with injected volume for stable slip (steady slip and fault creep), while we find a cubic relation for dynamic slip. Our results highlight that monitoring evolution of seismic moment release with injected volume in some cases may assist in discriminating between stable slip and unstable runaway ruptures.

Plain Language Summary Anthropogenic earthquakes caused by fluid injection have been reported worldwide to occur in the frame of waste-water disposal, CO_2 sequestration, and stimulation of hydrocarbon or deep geothermal reservoirs. To study the dynamics of injection-induced seismic energy release in a controlled environment, we performed laboratory fluid injection experiments on critically stressed high-permeability sandstone samples with a prefabricated fault. We monitored acoustic emission occurring during injection-induced fault sliding. We find that the total seismic deformation (expressed as total seismic moment) is related to total injected volume, independent of fault slip modes (i.e., dynamic slip, steady slip, and fault creep). Seismic moment release rate roughly scales with fault slip velocity. In our experiments, the fluid pressure front migrates faster than the rupture front by about 5 orders of magnitude, resulting in fault slip within a zone of homogeneous fluid overpressure. We find that cumulative seismic moment scales linearly with the injected volume for stable slip (steady slip and fault creep), while it follows a cubic relation for dynamic slip. Our experimental results suggest that the deviation of cumulative moment release with injected volume from a linear trend in practice might be a sign for potential seismic risk. This may be considered in modifying current injection strategies.

1. Introduction

It is widely acknowledged that fluid injection into the subsurface may induce earthquakes, as reported from waste-water disposal operations (Keranen et al., 2014), hydraulic fracturing in shale formations (Ellsworth, 2013), or in enhanced geothermal system (EGS) projects (Bentz et al., 2020). Fluid injection causes seismicity by diffusion of a pore pressure pulse (Shapiro & Dinske, 2009; Shapiro et al., 2002) and through poroelastic coupling to the rock matrix (Goebel et al., 2016, 2017; Segall & Lu, 2015). Rupture propagation has been analyzed using fracture mechanics (Galis et al., 2017; Garagash & Germanovich, 2012; Wang et al., 2016), and the process has been modeled numerically using a rate- and state-friction law (Cappa et al., 2018; Guglielmi et al., 2015). To mitigate potential seismic hazards associated with fluid injection, a better understanding of potential factors governing seismic moment release in response to fluid injection is of fundamental importance.

Assuming that fluid is injected into fully saturated formations, McGarr (2014) suggested a model providing an upper bound for cumulative and maximum seismic moments, which scale linearly with injected volume (ΔV_f). Galis et al. (2017) developed a fracture mechanics-based model to relate the size of stable, self-arrested ruptures to the injected volume by accounting for the rupture growing beyond the pressurized region. Their scaling relation suggests that the maximum seismic moment of self-arrested rupture scales with $\Delta V_f^{3/2}$. Based on statistical considerations, van der Elst et al. (2016) noted that for selected data sets, injected fluid volume controls total number of earthquakes, which in turn scales with maximum magnitude following a Gutenberg-Richter power law. Introducing a seismogenic index characterizing seismic activity arising from fluid injection (Shapiro et al., 2010), they proposed that the maximum seismic moment scales with $\Delta V_f^{3/2b}$ (van der Elst et al., 2016) and with the Gutenberg-Richter b value. Interestingly, for a commonly assumed $b = 1$, this model predicts a similar relation as suggested by Galis et al. (2017).

For the majority of past and present field-scale hydraulic stimulation projects, the trends of cumulative seismic moment with injected volume roughly show a linear relation but commonly remain below the upper bound of McGarr's model (Bentz et al., 2020). Interestingly, the corresponding slopes of maximum observed seismic moment versus cumulative injected volume in a double logarithmic plot range from 1 to 1.5 (Bentz et al., 2020), as predicted by the models of McGarr (2014) and Galis et al. (2017). This strongly suggests that the seismicity evolves in a stable way, at least for some period of the injection. In contrast, for the 2017 M_w 5.5 Pohang earthquake likely caused by hydraulic stimulation, seismic moment increased rapidly exceeding the upper bounds given by Galis et al. (2017), McGarr (2014), and van der Elst et al. (2016) due to occurrence of an unbound runaway rupture (Woo et al., 2019). Although the existing field-scale observations imply that the relation between moment release and injection parameters may depend on the dynamics of fault rupture and slip, the physical mechanisms governing rupture evolution and arrest remain poorly understood.

Our laboratory study aims at unraveling the characteristics of injection-induced seismic moment release from fault slip by reproducing different fault slip modes (i.e., dynamic slip, slip at constant rate, and fault creep) in response to different fluid pressurization rates. Our results suggest that the relation between seismic moment release and injected volume is strongly affected by fault slip modes.

2. Materials and Methods

2.1. Experimental Setup

We carefully performed fluid-driven fault slip tests on two sawcut cylindrical samples of Bentheim sandstone with dimensions of 50 mm in diameter and 100 mm in length. Each sample was prepared with a smooth sawcut fracture (polished, root-mean-square roughness of ~50 μm) inclined at $\theta = 30°$ relative to the cylinder axis and direction of maximum principal stress. The isotropic and homogeneous Bentheim sandstone composed of almost pure quartz (96.5%) has a high permeability of about 1 Darcy at ambient pressure (Wang, Dresen, et al., 2020), resulting in rapid fluid pressure diffusion. The samples were placed in rubber sleeves to isolate them from the confining oil. Experiments were conducted on critically stressed artificial faults at room temperature using a servo-controlled triaxial deformation apparatus (MTS, stiffness of machine plus assembly $K_{MTS} \approx 0.65 \times 10^9$ N/m or equivalent ~330 MPa/mm) equipped with a pore pressure system (see Figure S1 of the supporting information).

The samples were first loaded hydrostatically to a targeted confining pressure (σ_3) of 35 MPa while the pore pressure (P_P) was maintained constant at 5 MPa (Figure S2). Specimens were then axially loaded at a piston displacement rate of 1 μm/s to estimate maximum shear strength (τ_{ss}) resolved on the fault plane. Next, we slowly reduced axial stress (σ_1) until the shear stress resolved along fault plane is equal to about $0.92\tau_{ss}$. The position of the axial piston was kept constant, followed by fluid injection. Using two different fluid pressurization rates (i.e., 2 MPa/min in Test SC1 and 0.5 MPa/min in Test SC2, respectively, see Figure S3), fluid injection was increased stepwise from $P_P = 5$ MPa to $P_P = 29$ MPa by pumping distilled water to the bottom end of sample while the top end of sample is connected to a closed up-stream reservoir (undrained condition). Each fluid injection stage lasted for 10 min, composed of a 4 MPa ramp increment followed by a constant pressure plateau. Pore pressure increase of 4 MPa was achieved in 2 min in Test SC1 and in 8 min in Test SC2, respectively. Subsequently, P_P was kept constant for 8 min in Test SC1 and 2 min in Test SC2, respectively. Hydraulic energy (E_H) supplied by fluid injection over a time interval $[t_1, t_2]$ is as follows:

$$E_H = \int_{t_1}^{t_2} P_P Q dt, \tag{1}$$

where Q is fluid injection rate. In addition, an external linear variable displacement transducer (LVDT) located outside of the pressure vessel was used to measure the total axial displacement. We glued two pairs of orthogonal strain gages at the center of the hanging and footwall blocks of the sawcut sample cylinder to monitor the deformation of the rock matrix on both sides of the fault (Figure S4). Using the axial stress (σ_1) measured with an internal load cell, the shear stress (τ) and effective normal stress (σ_n') resolved on fault plane are as follows:

$$\tau = (\sigma_1 - \sigma_3)\sin\theta\cos\theta \tag{2}$$

$$\sigma_n^{'} = (\sigma_3 - P_p) + (\sigma_1 - \sigma_3)\sin^2\theta, \tag{3}$$

τ and σ_n' have been corrected for the contact area reduction between two blocks due to fault slip.

Fault displacement (u) is computed by projecting the net axial displacement that is determined from total axial displacement (Δl_{LVDT}) minus axial shortening of loading apparatus (Δl_{MTS}) and rock matrix (Δl_{RM}), as given:

$$u = \frac{\Delta l_{\mathrm{LVDT}} - \Delta l_{\mathrm{MTS}} - \Delta l_{\mathrm{RM}}}{\cos\theta}. \tag{4}$$

Δl_{MTS} is determined using $\Delta l_{\mathrm{MTS}} = \Delta F / K_{\mathrm{MTS}}$ where ΔF is the change of axial force. Δl_{RM} is estimated by $\Delta l_{\mathrm{RM}} = \varepsilon_1 L$ where ε_1 is the mean axial strain of two vertical strain gages attached to the center of rock specimen (Figure S4) and L is sample length. The slip velocity is thus taken as time derivative of slip displacement. Stress, strain, axial displacement, and injection data were synchronously recorded at a sampling rate of 10 Hz. More details on the experimental methods and loading procedures can be found in Wang, Kwiatek, et al. (2020).

2.2. Acoustic Emission Monitoring

Piezoelectric transducers (resonance frequency ~1 MHz) were directly mounted to the surface of samples to monitor acoustic emission (AE) events (microseismicity) during testing (Figure S4). AE signals recorded with 16 AE sensors in a triggered mode were amplified first by 40 dB using amplifiers with a built-in 100 kHz high-pass filter. Amplified waveforms were then continuously recorded at 10 MHz sampling frequency and digitized at 16-bit resolution. The arrival time and amplitude of first P wave for an individual AE event were picked automatically using the Akaike information criterion. To more accurately locate AE hypocenters, time-dependent anisotropic P wave velocities (due to stress-induced anisotropy) composed by five horizontal layers and one vertical layer were measured periodically at every 10 s using ultrasonic transmission pulses (Stanchits et al., 2011), resulting in a AE location accuracy of ±2 mm. Moment magnitude of AE (microseismicity) event (M_w^{AE}) is calculated using (Kwiatek, Goebel, & Dresen, 2014)

$$M_w^{AE} = \log_{10}\left(\frac{1}{n}\sum_{i=1}^{n}(A_i R_i)^2\right)^{0.5} - 10.5, \tag{5}$$

where A_i is the first P wave amplitude that was corrected for coupling quality of AE sensors and incidence angle using ultrasonic calibration technique (Kwiatek, Charalampidou, et al., 2014) and R_i is the source-receiver distance for sensor i. We use conversion factor of 10.5 from relative magnitude to absolute magnitude for our AE sensors. Resulting AE magnitudes and source parameters are in agreement with those parameters reported in previous studies (McLaskey & Lockner, 2014; Yoshimitsu et al., 2014). Using the relation between seismic moment (M_0) and moment magnitude (M_w) (Hanks & Kanamori, 1979)

$$M_w = \frac{2}{3}(\log_{10} M_0 - 9.1), \tag{6}$$

we estimated the cumulative seismic moment release detected by AE sensors by summing up all located AE events over a given time interval.

3. Results

3.1. Fault Slip Induced by Fluid Injection at Different Fluid Pressurization Rates

Initial loading of samples (Stage I) at $\sigma_3 = 35$ MPa and $P_P = 5$ MPa resulted in a linear increase of shear stress across the fault and sample compaction (Figures 1a and 1b). At the yield point, slip along the fault accelerated. Peak shear strength (τ_{ss}) of the sawcut samples was about 35 MPa. Once the peak stress was exceeded, the axial load was reduced and the axial piston was fixed at a shear stress corresponding to about $0.92\tau_{ss}$ (Stage II), and then fluid injection was started (Stage III). In the experiments, fault slip initiated shortly before the first fluid injection stage ended (at $P_P \approx 8.5$ MPa). Fluid injection at a pressurization rate of 2 MPa/min into Sample SC1 caused episodic slow stick-slip events (peak slip velocity <4 μm/s), accompanied by episodic stress drops and sharp peaks of AE activity (Figure 1a). In contrast, a fluid pressurization rate of 0.5 MPa/min in Test SC2 caused almost continuous fault creep with peak slip velocity <0.4 μm/s and a relatively constant AE rate (Figure 1b). Our observations highlight that the fluid-induced fault slip behavior is governed by fluid pressurization rates. However, comparisons of Tests SC1 and SC2 show that slip distance reached during each fluid injection stage and cumulative final fault slip (~1.5 mm) were very similar. Also, the amount of injected fluid and hydraulic energy was similar between tests (Figures 1c and 1d). In Test SC1, the occurrence of stick-slip was accompanied by a sudden spike-like increase in injection rate, which was not observed in Test SC2. This spike in injection rate was attributed to the abrupt pore pressure drop and stress relaxation with fault slip compensated by the fluid pressure system (Figure 1c). In contrast, in Test SC2 constant fluid injection rate resulted in steady fault creep (Figure 1d).

Slip evolution during fifth fluid injection stage in Test SC1 is shown in detail in Figure 1e. After fluid injection started, the fault remained locked until slip initiated (Phase A). This was followed by slip acceleration to peak velocity and deceleration (dynamic slip) (Phase B) and finally a long-lasting relaxation phase at constant slip-rate (steady slip) (Phase C). Upon shut-in of fluid injection, sliding stopped and the fault was locked again (Phase D). The time delay between start of fluid injection and slip onset decreased with progressive injection cycles (Figure S5). Steady slip (Phase C) was not observed in the first fluid injection stage because fluid injection was stopped shortly after the occurrence of stick-slip (Figure S5). In Test SC2 at lower pressurization rates fault creep rate was almost constant with only small perturbations during the short shut-in periods (Figures 1b and 1f).

3.2. Injection-Induced Seismic Moment Release

A total number of 3,983 and 3,331 AE events induced by fluid injection were located in tests SC1 and SC2, respectively. The AE events were located dominantly along the precut fault planes (Figure S6), indicating the robustness and accuracy of our AE hypocenter locations. Using Equation 5, the moment magnitudes of located AE events (M_w^{AE}) were found to span statistically from $M_w -9$ to $M_w -7$ (see Text S1 of the supporting information). This is in agreement with the previously reported AE source parameters from laboratory experiments (Goodfellow et al., 2015; McLaskey & Lockner, 2014; Yoshimitsu et al., 2014). In addition, the statistics of injection-induced AE events follow a Gutenberg-Richter frequency-magnitude relation with a b value of about 1.7 (see Text S1). The high b value ($b > 1$ is common for induced seismicity (van der Elst et al., 2016)) suggests that the van der Elst et al. (2016) model is no longer consistent with the Galis et al. (2017) model. Instead, it tends toward the slope predicted by the McGarr (2014) model.

Using Equation 6, we estimated the total seismic moment release (M_0^{AE}) from all AEs, which was about 1.39 and 1.35 N•m in Tests SC1 and SC2, respectively (Figure 2a). AE focal mechanisms are dominated by shear (double-couple) sources (Wang, Kwiatek, et al., 2020), suggesting that potential dilation or compaction deformation between two fault walls is negligible compared to shearing. For the injection-induced fault slip, we estimated total shear deformation moment (M_0^{def}) using $M_0^{def} = GAu$ where G is the shear modulus, A is the sawcut fault area and u is the average slip displacement. The shear deformation moment M_0^{def} represents the total combined seismic and aseismic deformation (McGarr & Barbour, 2018). With $G \approx 11$ GPa (Wang, Kwiatek, et al., 2020) and $A \approx 3{,}925$ mm^2, the total shear deformation moments induced by fluid injection for both tests sum up to similar values of about 2×10^4 N•m. The ratio of total M_0^{AE} to total M_0^{def} is about 7×10^{-5}. This is comparable to the values reported from in situ fluid injection experiments (De Barros et al., 2019; Guglielmi et al., 2015) and laboratory hydraulic fracturing tests (Goodfellow et al., 2015). This result implies that the injection-induced deformation is dominantly aseismic and thus

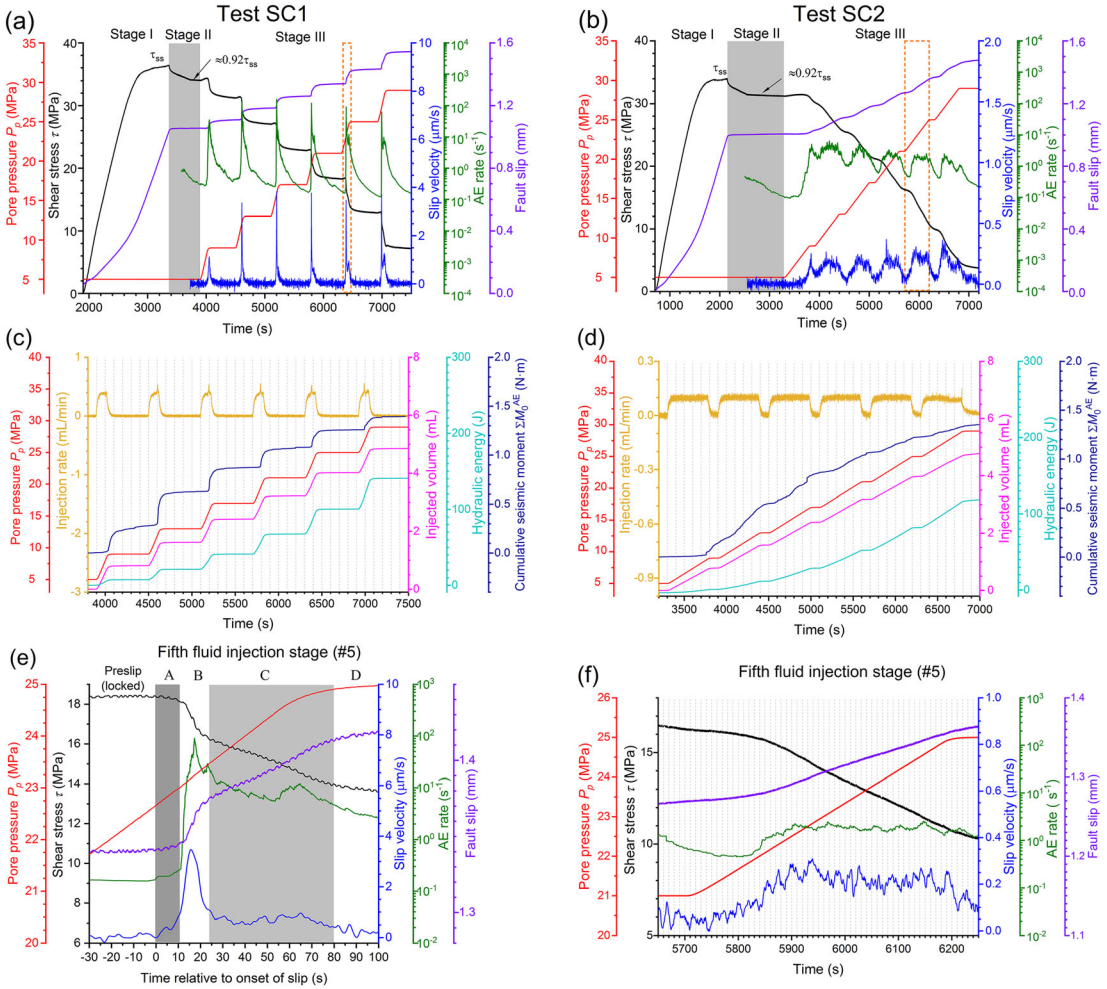

Figure 1. Temporal variation of pore pressure, shear stress, fault slip displacement, slip velocity, and AE rate in Tests SC1 (a) and SC2 (b), performed at pressurization rates of 2 and 0.5 MPa/min, respectively. After the peak shear strength (τ_{ss}) was achieved at steady state (Stage I), shear stress was then reduced to about $0.92\tau_{ss}$ (Stage II), followed by fluid injection (Stage III). (c and d) Evolution of pore pressure, injection rate, injected volume and hydraulic energy supplied, and cumulative seismic moment estimated from radiated AE events with elapsed time since fluid injection in Tests SC1 and SC2, respectively. (e and f) Zoomed details on induced fault slip during fifth fluid injection stage in Tests SC1 and SC2 (i.e., dashed orange rectangles in Figures 1a and 1b), respectively. Further details on the separation of fault slip states in Figure 1e are given in the text.

slow aseismic processes mainly occur outside the bandwidth of the AE recordings and below 100 kHz. The radiated seismic energy (E_s) can be estimated from seismic moment (M_0), static shear stress drop ($\Delta\tau$) and shear modulus (G) using $E_s = \Delta\tau M_0/2G$ (Hanks & Kanamori, 1979). Based on an average stress drop of about 26 MPa during entire fluid injection, the total seismic energy radiated in our tests corresponds to about 1.6×10^{-3} J. This results in a seismic injection efficiency (the ratio of seismic energy to hydraulic energy) of about 10^{-5}, consistent with the reported range from laboratory hydraulic fracture experiments (Goodfellow et al., 2015) and field-scale fluid injection operations (Bentz et al., 2020; Kwiatek et al., 2018).

The total ${M_0}^{AE}$ and total ${M_0}^{def}$ released during fluid injection are comparable in both tests. Total ${M_0}^{AE}$ release does not depend on fluid pressurization rate and fault slip modes, only on the total volume injected. In contrast, temporal evolution of cumulative seismic moment ($\sum {M_0}^{AE}$) and cumulative shear deformation moment ($\sum {M_0}^{def}$) differs between the different tests and clearly is affected by pressurization rates and slip modes. The $\sum {M_0}^{def}$ increases almost linearly with hydraulic energy, but $\sum {M_0}^{AE}$ shows a nonlinear increase with hydraulic energy (Figure 2b). The release of $\sum {M_0}^{AE}$ first increases linearly with fault slip in both tests and then shows a slow increase (Figure 2c). This may be caused by stress relaxation associated with fault slip

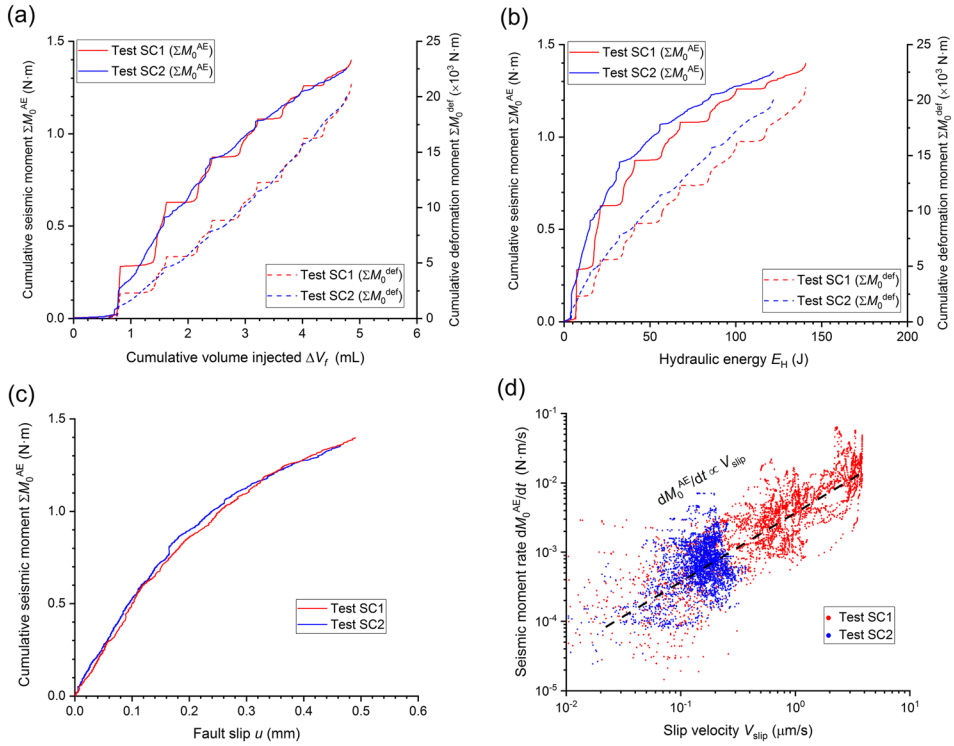

Figure 2. The evolution of cumulative seismic moment ($\sum M_0{}^{\mathrm{AE}}$) estimated from radiated AE events and cumulative shear deformation moment ($\sum M_0{}^{\mathrm{def}}$) derived from fault slip as a function of (a) cumulative injected volume (ΔV_f) and (b) hydraulic energy (E_H). (c) Evolution of cumulative seismic moment ($\sum M_0{}^{\mathrm{AE}}$) with increasing fault slip displacement (u) since fluid injection. (d) Relation between seismic moment release rate ($dM_0{}^{\mathrm{AE}}/dt$) and fault slip velocity (V_{slip}).

and/or by fault lubrication arising from progressively generated wet fault gouge, likely reducing roughness and asperities between two fault blocks. Additionally, seismic moment release rate from AE is clearly related to slip velocity (Figure 2d).

In Test SC1, $\sum M_0{}^{\mathrm{AE}}$ and $\sum M_0{}^{\mathrm{def}}$ initially increase slowly during slip initiation (Figures 3a and 3b). As slip velocity ramps up, we find a cubic relation ($M_0^{AE} \propto \Delta V_f^3$ and $M_0^{def} \propto \Delta V_f^3$), which changes into a linear relation after slip rate decreases to almost constant. This is in contrast to Test SC2 (Figures 3c and 3d) that displays roughly a linear relation between cumulative moments and injected fluid volume for the entire duration of fluid injection and fault slip.

4. Discussion

4.1. Migration of Rupture Front and Fluid Pressure Front and Potential Impacts on Injection-Induced Moment Release

Recently, it has been suggested that fluid injection into a shallow crustal fault zone (Bhattacharya & Viesca, 2019; De Barros et al., 2016) and during hydraulic fracturing operations (Eyre et al., 2019) may first activate aseismic slip leading to seismic ruptures that extend beyond the pressurized region. A rupture front outpacing pore pressure migration has also been modeled numerically (Cappa et al., 2018, 2019; Wynants-Morel et al., 2020). We estimated migration of a fluid pressure front along the sawcut fault plane by solving the pressure diffusion equation for the conditions of our experiments (see Text S2). The permeability of porous Bentheim sandstone is high (~1 Darcy), resulting in rapid migration of the pore pressure front with an average speed of about 10^3 m/s. This is supported by the observed almost equal fluid pressures monitored at the two ends of samples (Figure S2).

The AEs originating from breaking of asperities on the fault plane since the onset of fault slip reflect the microfracturing process occurring within fault patches. We assume that migration of the rupture zone is

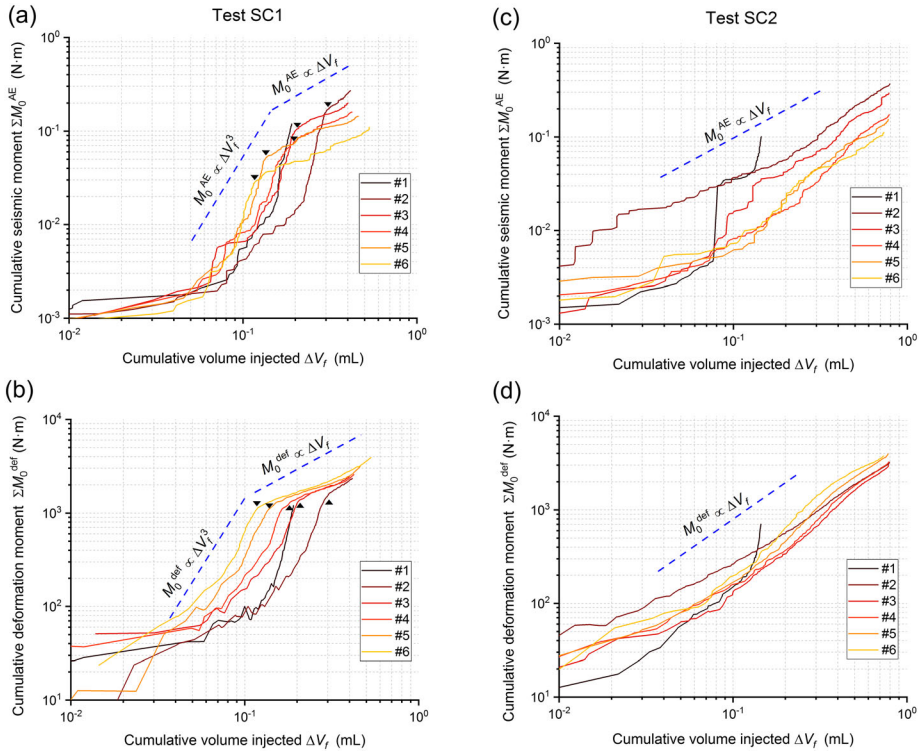

Figure 3. The evolution of (a) cumulative seismic moment ($\sum {M_0}^{\mathrm{AE}}$) and (b) cumulative shear deformation moment ($\sum {M_0}^{\mathrm{def}}$) as a function of injected volume (ΔV_{f}) since onset of fault slip during each fluid injection stage in Test SC1. The black triangles denote the transition from dynamic slip (e.g., Phase B in Figure 1e) to steady slip (e.g., Phase C in Figure 1e) during second to sixth fluid injection stages in Test SC1. Except first fluid injection stage, the evolution of (c) cumulative seismic moment ($\sum {M_0}^{\mathrm{AE}}$) and (d) cumulative shear deformation moment ($\sum {M_0}^{\mathrm{def}}$) as a function of injected volume (ΔV_{f}) during the later fluid injection stages in Test SC2 due to the occurrence of continuous fault creep. For first fluid injection stage in Test SC2, only the data since onset of fault slip were used.

indicated by migration of AE hypocenters across the fault resulting from breaking grain-scale asperities (Lockner et al., 1991). Using a clustering algorithm of *density-based spatial clustering of applications with noise* (DBSCAN) (Ester et al., 1996), the temporal evolution of the AE spreading area (see Text S3) and inferred rupture length (see Text S4) since onset of slip can be quantitatively estimated. The rupture velocity is estimated to be only about 7 and 0.4 mm/s in Tests SC1 and SC2, respectively (see Text S4). Compared to the much faster propagation rate of the fluid pressure front, this suggests that rupture propagation occurs entirely within a fluid-pressurized fault region.

Rupture propagation and sliding are caused by the increase in fluid pressure reducing effective normal stress and frictional strength acting on the fault. For a similar injection scenario, McGarr (2014) developed a model proposing an upper bound for cumulative moment release ($\sum M_0$) linearly increasing with injected volume (ΔV_f): $\sum M_0 = 2G\Delta V_f$. For stable rupture propagation, we find $M_0 \propto T$ (Figure S7), similar to what has been suggested for moment-duration scaling of slow slip events (Gomberg et al., 2016; Ide et al., 2007). In contrast, for dynamic slip events in Test SC1 we observe $M_0 \propto T^3$ scaling as commonly found for earthquakes (Figure S7). Since flow rate is kept almost constant during injection periods, seismic moment grows linearly with injected volume ($M_0 \propto \Delta V_f$) during stable slip (constant slip rate and fault creep), as predicted by McGarr (2014). A scaling of $M_0 \propto \Delta V_f^3$ is also derived for unstable and dynamic slip, as shown in Figures 3a and 3b.

The competition between rupture propagation and fluid pressure migration is complex depending on many factors, such as hydraulic conductivity (Cappa et al., 2018), spatially varied frictional properties (Cappa et al., 2019), initial stress state of fault zones (Wynants-Morel et al., 2020), and fault roughness (Maurer et al., 2020). In our experiments, the fluid pressure front propagates very fast along the highly

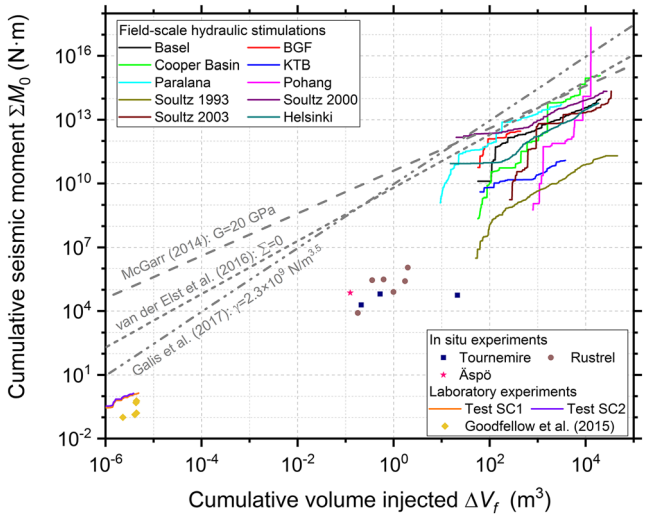

Figure 4. Temporal evolution of cumulative seismic moment with injected volume across a wide range of scales from field hydraulic stimulations to laboratory experiments. Note that the seismic moment is determined either from radiated seismic waves during in situ and field tests or from the radiated acoustic emission events during laboratory tests. The data sets of field-scale hydraulic stimulation projects are from Bentz et al. (2020). The collected projects include Basel, Berlin geothermal field (BGF), Cooper Basin, German deep scientific drilling hole (KTB), Paralana, Pohang, Soultz-sous-Forêts, and Helsinki. The scatter points of in situ and laboratory experiments indicate the total seismic moment release and total injected volume at the termination of fluid injection. The in situ fluid injection experiments performed at the Underground Laboratory of Tournemire (France) and at the Underground Laboratory of Rustrel (France) are from De Barros et al. (2019), and the in situ hydraulic fracturing experiments performed at the Underground Äspö Hard Rock Laboratory (Sweden) are in Kwiatek et al. (2018). The laboratory hydraulic fracturing tests by Goodfellow et al. (2015) are also included. The theoretical limit to cumulative seismic moment predicted by McGarr (2014) assuming shear modulus (G) of 20 GPa is indicated by the gray long-dash line. The gray short-dash line denotes the corresponding prediction from van der Elst et al. (2016) in which the seismogenic index Σ and b value are set to 0 and 1.2, respectively. The gray dash-dot line refers to the upper bound suggested by Galis et al. (2017) assuming $\gamma = 2.3 \times 10^9$ N/m$^{3.5}$. Details on the equations from van der Elst et al. (2016) and Galis et al. (2017) can be found in Text S5 of the supporting information.

permeable fault zone and rock matrix outpacing the front of slow fault slip. It is conceivable that for low-permeability fault zones and fast ruptures this relation may be reversed. Corresponding observations do exist from fault reactivation experiments (Bhattacharya & Viesca, 2019; Eyre et al., 2019).

4.2. What Causes the Transition from Dynamic Slip to Steady Slip at a High Fluid Pressurization Rate?

In Test SC1, we notice a transition from dynamic slip (e.g., Phase B in Figure 1e) to slip at constant rate (e.g., Phase C in Figure 1e) during later fluid injection stages (Figure S5). This transition may be related to two independent factors. The fast pressurization rate applied in Test SC1 rapidly decreases fault frictional strength exceeding the rise time of the loading system (Shimamoto et al., 1980). Accelerated stress relaxation of the loaded system-sample assembly and release of the energy stored in the sample-machine system will occur. As the machines stiffness (~330 MPa/mm) exceeds the fault stiffness (~60 MPa/mm) (Wang, Kwiatek, et al., 2020), fault slip remains stable and continues as long as fluid is injected reducing fault strength. In contrast, the slow fluid pressurization rate in Test SC2 allows for almost simultaneous stress relaxation and equilibration of applied shear stress with reduced fault strength, resulting in continuous and steady fault creep.

In addition, fault slip mode could be affected by fault geometry (Gomberg et al., 2016). Specifically, the transition from dynamic slip to steady slip corresponds to the change from unbounded to bounded rupture when the rupture area reaches the sample boundaries. In Test SC1, the termination of dynamic slip occurs shortly before the rupture propagation has progressed across the entire fault plane, as indicated by the spreading process of AE hypocenters over time (see Text S4 and Figure S12). Subsequent slip occurs unidirectionally along a bounded slip plane.

4.3. Implications for Fluid-Induced Seismicity

Seismic moment release in laboratory experiments, in situ tests, and many field-scale hydraulic stimulations are well constrained by the upper bound suggested by the McGarr (2014) model (Figure 4). In addition, our laboratory experiments show that the injected volume limits the total deformation moment release once the aseismic moment is also taken into account (see Figure S15), in agreement with laboratory hydraulic fracture experiments by Goodfellow et al. (2015) (McGarr & Barbour, 2018). In contrast to the McGarr (2014) model, the predictions from van der Elst et al. (2016) and Galis et al. (2017) models appear to be more consistent with laboratory-scale results at low injected volumes.

Our laboratory experiments highlight that although we do not change the total moment release caused by fluid injection, there are now clear indications that it may be possible to manually govern the seismic moment release rate that depends on fault slip modes by varying fluid pressurization rates. This is also supported by the observed induced seismicity correlated with variation of waste-water injection rate in Oklahoma (Langenbruch & Zoback, 2016) and by the recent successful field tests of controlling seismic activity in EGS projects (Kwiatek et al., 2019) by adjusting injection parameters during a pressure-controlled, stable injection phase. The monitored response of linear moment release with ongoing injected volume for field projects is believed to be indicative of stable rupture (Bentz et al., 2020), which is in agreement with our experimental results.

The moment-volume relation observed in our experiments is drawn from the scenario of injection-induced fault slip confined within a homogeneous pressurized region. In striking contrast to well-controlled laboratory experiments, the geological setting of reservoir-scale injection projects in many cases may be not

properly confined and even some hidden faults nearby may not be known in advance (Eyre et al., 2019; Rathnaweera et al., 2020). Nevertheless, it appears that a linear relation of moment - injected volume for stable slip is found in different geological settings by monitoring evolution of moment release at many field-scale fluid injection projects (Figure 4). For the 2017 M_w 5.5 Pohang/South Korea earthquake, a steep increase in moment release exceeding upper bounds predicted by McGarr (2014), van der Elst et al. (2016), and Galis et al. (2017) models suggests early occurrence of unstable runaway rupture, resulting in a rapid release of seismic moment (Figure 4).

To better predict injection-induced moment release on reservoir scale, the knowledge of background stress, fault roughness, hydraulic conductivity, and frictional properties at the injection site is essential. This would allow us to estimate the evolution of fluid pressure migration and induced rupture propagation with time. Special attention should be paid to a scenario of rupture front propagating beyond the pressurized region. The development of ruptured area beyond the pressurized region may not be driven directly by fluid pressure change but by shear stress transfer due to aseismic slip (Bhattacharya & Viesca, 2019; Eyre et al., 2019), not captured by existing evaluation methods based on pure fluid pressure diffusion models (e.g., Shapiro & Dinske, 2009; Shapiro et al., 2002). Real-time monitoring of temporal evolution of seismic moment release with injected volume and promptly evaluating the current seismic risks may allow to adapt injection parameters and partially control seismic activity during a stable, pressure-controlled injection phase, as observed at many injection sites.

5. Conclusion

We performed laboratory fluid injection experiments on critically stressed sawcut sandstone samples with a high permeability at different fluid pressurization rates. Episodic slow stick-slip events are induced at high fluid pressurization rate while fault creep occurs in response to slow fluid pressurization rate. Fluid-induced fault deformation is dominantly aseismic. The released total seismic moment is found to be related to total injected volume, independent of fault slip behavior. Seismic moment release rate of AEs is related to measured fault slip velocity. In our experiments, the fluid pressure migration is faster than rupture propagation by about 5 orders of magnitude, resulting in induced fault slip fully confined within a homogenous pressurized zone. The relation between cumulative moment release and injected volume is affected by fault slip behavior, characterized by a linear relation for slip at constant rate and fault creep while a cubic relation for unstable and dynamic slip. Our experimental results suggest that early deviation of cumulative moment release with injected volume from a linear trend should be scrutinized carefully in stimulations.

Data Availability Statement

The data set of seismic moment in this study can be found at Mendeley Data (https://doi.org/10.17632/cbhrs6d8rr.1), and the rest of data sets have been archived at GFZ Data Services (http://doi.org/10.5880/GFZ.4.2.2020.002).

Acknowledgments
The authors thank Stefan Gehrmann for sample preparation and Michael Naumann for assistance with laboratory experiments in MTS apparatus. Audrey Bonnelye is appreciated for providing useful comments on the original manuscript. We thank Andrew J. Barbour for constructive comments and suggestions that significantly improved the manuscript. L. Wang acknowledges China Scholarship Council for providing funding to perform this study at GFZ. This manuscript is accompanied by supporting information.

References

Bentz, S., Kwiatek, G., Martínez-Garzón, P., Bohnhoff, M., & Dresen, G. (2020). Seismic moment evolution during hydraulic stimulations. *Geophysical Research Letters*, *47*, e2019GL086185. https://doi.org/10.1029/2019GL086185

Bhattacharya, P., & Viesca, R. C. (2019). Fluid-induced aseismic fault slip outpaces pore-fluid migration. *Science*, *364*(6439), 464–468. https://doi.org/10.1126/science.aaw7354

Cappa, F., Guglielmi, Y., Nussbaum, C., & Birkholzer, J. (2018). On the relationship between fault permeability increases, induced stress perturbation, and the growth of aseismic slip during fluid injection. *Geophysical Research Letters*, *45*, 1111–1220. https://doi.org/10.1029/2018GL080233

Cappa, F., Scuderi, M. M., Collettini, C., Guglielmi, Y., & Avouac, J.-P. (2019). Stabilization of fault slip by fluid injection in the laboratory and in situ. *Science Advances*, *5*(3), eaau4065. https://doi.org/10.1126/sciadv.aau4065

De Barros, L., Cappa, F., Guglielmi, Y., Duboeuf, L., & Grasso, J. R. (2019). Energy of injection-induced seismicity predicted from in-situ experiments. *Scientific Reports*, *9*(1), 4999. https://doi.org/10.1038/s41598-019-41306-x

De Barros, L., Daniel, G., Guglielmi, Y., Rivet, D., Caron, H., Payre, X., et al. (2016). Fault structure, stress, or pressure control of the seismicity in shale? Insights from a controlled experiment of fluid-induced fault reactivation. *Journal of Geophysical Research: Solid Earth*, *121*, 4506–4522. https://doi.org/10.1002/2015JB012633

Ellsworth, W. L. (2013). Injection-induced earthquakes. *Science*, *341*(6142), 1225942. https://doi.org/10.1126/science.1225942

Ester, M., Kriegel, H.-P., Sander, J., & Xu, X. (1996). A density-based algorithm for discovering clusters in large spatial databases with noise. In *Proceedings of the Second International Conference on Knowledge Discovery and Data Mining (KDD-96)* (pp. 226–231). AAAI.

Eyre, T. S., Eaton, D. W., Garagash, D. I., Zecevic, M., Venieri, M., Weir, R., & Lawton, D. C. (2019). The role of aseismic slip in hydraulic fracturing–induced seismicity. *Science Advances*, *5*(8), eaav7172. https://doi.org/10.1126/sciadv.aav7172

Galis, M., Ampuero, J. P., Mai, P. M., & Cappa, F. (2017). Induced seismicity provides insight into why earthquake ruptures stop. *Science Advances*, *3*(12), eaap7528. https://doi.org/10.1126/sciadv.aap7528

Garagash, D. I., & Germanovich, L. N. (2012). Nucleation and arrest of dynamic slip on a pressurized fault. *Journal of Geophysical Research*, *117*, B10310. https://doi.org/10.1029/2012JB009209

Goebel, T. H. W., Hosseini, S. M., Cappa, F., Hauksson, E., Ampuero, J. P., Aminzadeh, F., & Saleeby, J. B. (2016). Wastewater disposal and earthquake swarm activity at the southern end of the Central Valley, California. *Geophysical Research Letters*, *43*, 1092–1099. https://doi.org/10.1002/2015GL066948

Goebel, T. H. W., Weingarten, M., Chen, X., Haffener, J., & Brodsky, E. E. (2017). The 2016 *Mw*5.1 Fairview, Oklahoma earthquakes: Evidence for long-range poroelastic triggering at >40 km from fluid disposal wells. *Earth and Planetary Science Letters*, *472*, 50–61. https://doi.org/10.1016/j.epsl.2017.05.011

Gomberg, J., Wech, A., Creager, K., Obara, K., & Agnew, D. (2016). Reconsidering earthquake scaling. *Geophysical Research Letters*, *43*, 6243–6251. https://doi.org/10.1002/2016GL069967

Goodfellow, S. D., Nasseri, M. H. B., Maxwell, S. C., & Young, R. P. (2015). Hydraulic fracture energy budget: Insights from the laboratory. *Geophysical Research Letters*, *42*, 3179–3187. https://doi.org/10.1002/2015GL063093

Guglielmi, Y., Cappa, F., Avouac, J.-P., Henry, P., & Elsworth, D. (2015). Seismicity triggered by fluid injection-induced aseismic slip. *Science*, *348*(6240), 1224–1226. https://doi.org/10.1126/science.aab0476

Hanks, T. C., & Kanamori, H. (1979). A moment magnitude scale. *Journal of Geophysical Research*, *84*(B5), 2348–2350. https://doi.org/10.1029/JB084iB05p02348

Ide, S., Beroza, G. C., Shelly, D. R., & Uchide, T. (2007). A scaling law for slow earthquakes. *Nature*, *447*(7140), 76–79. https://doi.org/10.1038/nature05780

Keranen, K. M., Weingarten, M., Abers, G. A., Bekins, B. A., & Ge, S. (2014). Sharp increase in central Oklahoma seismicity since 2008 induced by massive wastewater injection. *Science*, *345*(6195), 448–451. https://doi.org/10.1126/science.1255802

Kwiatek, G., Charalampidou, E.-M., Dresen, G., & Stanchits, S. (2014). An improved method for seismic moment tensor inversion of acoustic emissions through assessment of sensor coupling and sensitivity to incidence angle. *International Journal of Rock Mechanics and Mining Sciences*, *65*, 153–161. https://doi.org/10.1016/j.ijrmms.2013.11.005

Kwiatek, G., Goebel, T. H. W., & Dresen, G. (2014). Seismic moment tensor and b value variations over successive seismic cycles in laboratory stick-slip experiments. *Geophysical Research Letters*, *41*, 5838–5846. https://doi.org/10.1002/2014GL060159

Kwiatek, G., Martínez-Garzón, P., Plenkers, K., Leonhardt, M., Zang, A., von Specht, S., et al. (2018). Insights into complex subdecimeter fracturing processes occurring during a water injection experiment at depth in Äspö Hard Rock Laboratory, Sweden. *Journal of Geophysical Research: Solid Earth*, *123*, 6616–6635. https://doi.org/10.1029/2017JB014715

Kwiatek, G., Saarno, T., Ader, T., Bluemle, F., Bohnhoff, M., Chendorain, M., et al. (2019). Controlling fluid-induced seismicity during a 6.1-km-deep geothermal stimulation in Finland. *Science Advances*, *5*(5), eaav7224. https://doi.org/10.1126/sciadv.aav7224

Langenbruch, C., & Zoback, M. D. (2016). How will induced seismicity in Oklahoma respond to decreased saltwater injection rates? *Science Advances*, *2*(11), e1601542. https://doi.org/10.1126/sciadv.1601542

Lockner, D. A., Byerlee, J. D., Kuksenko, V., Ponomarev, A., & Sidorin, A. (1991). Quasi-static fault growth and shear fracture energy in granite. *Nature*, *350*(6313), 39–42. https://doi.org/10.1038/350039a0

Maurer, J., Dunham, E. M., & Segall, P. (2020). Role of fluid injection on earthquake size in dynamic rupture simulations on rough faults. *Geophysical Research Letters*, *47*, e2020GL088377. https://doi.org/10.1029/2020GL088377

McGarr, A. (2014). Maximum magnitude earthquakes induced by fluid injection. *Journal of Geophysical Research: Solid Earth*, *119*, 1008–1019. https://doi.org/10.1002/2013JB010597

McGarr, A., & Barbour, A. J. (2018). Injection-induced moment release can also be aseismic. *Geophysical Research Letters*, *45*, 5344–5351. https://doi.org/10.1029/2018GL078422

McLaskey, G. C., & Lockner, D. A. (2014). Preslip and cascade processes initiating laboratory stick slip. *Journal of Geophysical Research: Solid Earth*, *119*, 6323–6336. https://doi.org/10.1002/2014JB011220

Rathnaweera, T. D., Wu, W., Ji, Y., & Gamage, R. P. (2020). Understanding injection-induced seismicity in enhanced geothermal systems: From the coupled thermo-hydro-mechanical-chemical process to anthropogenic earthquake prediction. *Earth-Science Reviews*, *205*, 103182. https://doi.org/10.1016/j.earscirev.2020.103182

Segall, P., & Lu, S. (2015). Injection-induced seismicity: Poroelastic and earthquake nucleation effects. *Journal of Geophysical Research: Solid Earth*, *120*, 5082–5103. https://doi.org/10.1002/2015JB012060

Shapiro, S. A., & Dinske, C. (2009). Scaling of seismicity induced by nonlinear fluid-rock interaction. *Journal of Geophysical Research*, *114*, B09307. https://doi.org/10.1029/2008JB006145

Shapiro, S. A., Dinske, C., Langenbruch, C., & Wenzel, F. (2010). Seismogenic index and magnitude probability of earthquakes induced during reservoir fluid stimulations. *The Leading Edge*, *29*(3), 304–309. https://doi.org/10.1190/1.3353727

Shapiro, S. A., Rothert, E., Rath, V., & Rindschwentner, J. (2002). Characterization of fluid transport properties of reservoirs using induced microseismicity. *Geophysics*, *67*(1), 212–220. https://doi.org/10.1190/1.1451597

Shimamoto, T., Handin, J., & Logan, J. M. (1980). Specimen-apparatus interaction during stick-slip in a tri axial compression machine: A decoupled two-degree-of-freedom model. *Tectonophysics*, *67*(3), 175–205. https://doi.org/10.1016/0040-1951(80)90234-6

Stanchits, S., Mayr, S., Shapiro, S., & Dresen, G. (2011). Fracturing of porous rock induced by fluid injection. *Tectonophysics*, *503*(1–2), 129–145. https://doi.org/10.1016/j.tecto.2010.09.022

van der Elst, N. J., Page, M. T., Weiser, D. A., Goebel, T. H. W., & Hosseini, S. M. (2016). Induced earthquake magnitudes are as large as (statistically) expected. *Journal of Geophysical Research: Solid Earth*, *121*, 4575–4590. https://doi.org/10.1002/2016JB012818

Wang, L., Bai, B., Li, X., Liu, M., Wu, H., & Hu, S. (2016). An analytical model for assessing stability of pre-existing faults in Caprock caused by fluid injection and extraction in a reservoir. *Rock Mechanics and Rock Engineering*, *49*(7), 2845–2863. https://doi.org/10.1007/s00603-016-0933-0

Wang, L., Dresen, G., Rybacki, E., Bonnelye, A., & Bohnhoff, M. (2020). Pressure-dependent bulk compressibility of a porous granular material modeled by improved contact mechanics and micromechanical approaches: Effects of surface roughness of grains. *Acta Materialia*, *188*, 259–272. https://doi.org/10.1016/j.actamat.2020.01.063

Wang, L., Kwiatek, G., Rybacki, E., Bonnelye, A., Bohnhoff, M., & Dresen, G. (2020). Laboratory study on fluid-induced fault slip behavior: The role of fluid pressurization rate. *Geophysical Research Letters*, *46*, e2019GL086627. https://doi.org/10.1029/2019GL086627

Woo, J.-U., Kim, M., Sheen, D. H., Kang, T. S., Rhie, J., Grigoli, F., et al. (2019). An in-depth seismological analysis revealing a causal link between the 2017 *MW* 5.5 Pohang earthquake and EGS project. *Journal of Geophysical Research: Solid Earth*, *124*, 13,060–13,078. https://doi.org/10.1029/2019JB018368

Wynants-Morel, N., Cappa, F., De Barros, L., & Ampuero, J.-P. (2020). Stress perturbation from aseismic slip drives the seismic front during fluid injection in a permeable fault. *Journal of Geophysical Research: Solid Earth*, *125*, e2019JB019179. https://doi.org/10.1029/2019JB019179

Yoshimitsu, N., Kawakata, H., & Takahashi, N. (2014). Magnitude −7 level earthquakes: A new lower limit of self-similarity in seismic scaling relationships. *Geophysical Research Letters*, *41*, 4495–4502. https://doi.org/10.1002/2014GL060306

References From the Supporting Information

Aki, K., & Richards, P. G. (1980). *Quantitative seismology: Theory and methods*. San Francisco, CA: Freeman, Cooper.

Bayart, E., Svetlizky, I., & Fineberg, J. (2016). Fracture mechanics determine the lengths of interface ruptures that mediate frictional motion. *Nature Physics*, *12*(2), 166–170. https://doi.org/10.1038/nphys3539

Bizzarri, A. (2012). Rupture speed and slip velocity: What can we learn from simulated earthquakes? *Earth and Planetary Science Letters*, *317–318*, 196–203. https://doi.org/10.1016/j.epsl.2011.11.023

Jaeger, J. C., Cook, N. G. W., & Zimmerman, R. (2009). *Fundamentals of rock mechanics*. Hoboken: John Wiley & Sons.

Ke, C.-Y., McLaskey, G. C., & Kammer, D. S. (2018). Rupture termination in laboratory-generated earthquakes. *Geophysical Research Letters*, *45*, 12,712–784,792. https://doi.org/10.1029/2018GL080492

Polyanin, A. D. (2002). *Linear partial differential equations for engineers and scientists*. New York: Chapman and Hall/CRC.